Domain-Wall Damping in Ultrathin Nanostripes with Dzyaloshinskii-Moriya Interaction

Oleksii M. Volkov,[1,*] Florian Kronast,[2] Claas Abert,[3,4] Eduardo Sergio Oliveros Mata,[1] Tobias Kosub,[1] Pavlo Makushko,[1,5] Denise Erb,[1] Oleksandr V. Pylypovskyi,[1,6] Mohamad-Assaad Mawass,[2] Denis Sheka,[7] Shengqiang Zhou,[1] Jürgen Fassbender,[1] and Denys Makarov[1,†]

[1] *Helmholtz-Zentrum Dresden - Rossendorf e.V., Institute of Ion Beam Physics and Materials Research, Bautzner LandStr. 400, Dresden 01328, Germany*

[2] *Helmholtz-Zentrum Berlin für Materialien und Energie, Albert-Einstein-Str. 15, Berlin 12489, Germany*

[3] *Faculty of Physics, University of Vienna, Universitätsring 1, Wien 1010, Austria*

[4] *University of Vienna Research Platform MMM Mathematics – Magnetism – Materials, University of Vienna, Universitätsring 1, Wien 1010, Austria*

[5] *National Technical University of Ukraine "Igor Sikorsky Kyiv Polytechnic Institute", Peremohy Avenue 37, Kyiv 03056, Ukraine*

[6] *Kyiv Academic University, Vernadsky Boulevard, 36, Kyiv 03142, Ukraine*

[7] *Department of Mathematics and Theoretical Radio Physics, Faculty of Radio Physics, Electronics and Computer Systems, Taras Shevchenko National University of Kyiv, Volodymyrska Street, 60, Kyiv 01601, Ukraine*

(Received 4 September 2020; revised 9 December 2020; accepted 12 February 2021; published 12 March 2021)

Asymmetrically sandwiched thin magnetic layers with perpendicular anisotropy and Dzyaloshinskii-Moriya interaction (DMI) is the prospective material science platform for spin-orbitronic technologies that rely on the motion of chiral magnetic textures, like skyrmions or chiral domain walls (DWs). The dynamic performance of a DW-based racetrack is defined by the strength of the DMI and the DW damping. The determination of the latter parameter is typically done based on technically challenging DW motion experiments. Here, we propose a method to access both the DMI constant and DW damping from static experiments by monitoring the tilt of magnetic DWs in nanostripes. We experimentally demonstrate that in perpendicularly magnetized //CrO_x/Co/Pt stacks, DWs can be trapped on edge roughness in a metastable tilted state as a result of the DW dynamics driven by an external magnetic field. The measured tilt can be correlated to the DMI strength and DW damping in a self-consistent way in the frame of a theoretical formalism based on the collective coordinate approach.

DOI: 10.1103/PhysRevApplied.15.034038

I. INTRODUCTION

Structural inversion symmetry breaking in low-dimensional ultrathin magnetic multilayers determines electronic and magnetic properties at interfaces [1–5]. If ultrathin ferromagnetic layers are brought in contact with a nonmagnetic heavy metal with a strong spin-orbit coupling, Dzyaloshinskii-Moriya interaction (DMI) will appear [1–3,6,7] in addition to a perpendicular magnetic anisotropy. This leads to the stabilization of chiral noncollinear magnetic textures, e.g., skyrmions [4,8–11], skyrmion bubbles [12], and chiral domain walls (DWs) [13,14]. Beside emerging fundamental effects, such as the occurrence of skyrmion [5,9,15–17] and topological [9,18] Hall effects, the fast motion of chiral DWs [14,19] and skyrmions [10,11,16] is the key enabler of prospective memory and logic devices operating based on spin-orbit torques [5,16,19–22].

The performance of spin-orbitronic devices is determined by the static and dynamic micromagnetic parameters [19,23]. In particular, the speed of a DW-based racetrack is defined by the strength of the field or spin-polarized current driving the DW, as well as the DMI constant, D, and the DW damping parameter, α [19,24]. The necessity of having a strong DMI requires ultrathin magnetic layers with thicknesses in the range of 1 nm. Those thin films are usually polycrystalline, which often reduces the structural quality of the layer stack. Structural imperfections, in addition to the spin pumping mechanism [25–27] that arises due to the proximity of a ferromagnet with a heavy metal, lead to an enhanced DW damping. For Co-based sandwiches, $\alpha = 0.1 \div 0.4$ [28,29], which is at least one order of magnitude larger

*o.volkov@hzdr.de
†d.makarov@hzdr.de

than for bulk Co ($\alpha = 0.005 \div 0.01$) [30,31]. Accessing α typically requires dynamic experiments on the motion of DWs in confined geometries [32]. The interpretation of these results can be cumbersome, especially if experiments are done in the creep regime of the DW motion [33–35], which is usual for ultrathin stripes with pronounced pinning. Strong damping accompanied by week signals from ultrathin films might account for difficulties in determining the DMI constant by spectroscopy-based approaches (e.g., Brillouin light scattering) [36,37].

Here, we present an experimental method for the quantification of the DW damping parameter and the DMI constant from the static investigations of magnetic field manipulated changes in the DWs morphology. Namely, we observe a persistent tilt of the DW plane in equilibrium due to a pronounced pinning of DWs on structural inhomogeneities [Fig. 1(a)]. By analyzing the DW tilts induced by different magnetic fields, it is possible to determine self-consistently the range of DW damping parameters and DMI constants for the particular layer stack. We validate this method on the perpendicularly magnetized //CrO_x/Co/Pt nanostripes with the surface-induced DMI. The DW tilt is a dynamic effect that arises as a result of the interplay between the external field driving and the surface-induced DMI [24]. In polycrystalline samples that possess spatial variation of magnetic parameters (e.g., uniaxial anisotropy, K_0), a moving DW can be trapped in a tilted state after the external driving field is switched off. The statistical analysis of the DW tilt angles combined with the theoretical model in the frame of the collective coordinate approach [24,38,39] allows one to self-consistently determine the DMI strength and DW damping. In our work, using two reference fields, which provide two characteristic tilt angles, allow us to retrieve the range of DMI strengths $D \geq 0.8$ mJ/m^2 and DW damping parameters $\alpha \geq 0.1$. The upper limit for the DMI constant agrees with an independent transport-based measurement giving $D_0 = 0.90 \pm 0.13$ mJ/m^2. Using this refined DMI value, we provide a better estimate for the damping parameter $\alpha = 0.13 \pm 0.02$. This value lies in a typical DW damping range for the Co-based asymmetrical layer stacks that are obtained from dynamic experiments [28,29]. In this respect, the combination of the proposed method with standard metrological techniques opens up opportunities for the quantification of both static and dynamic micromagnetic parameters based on static magnetization measurements of the DWs morphology.

II. RESULTS

We prepare asymmetric //CrO_x(5 nm)/Co(1.0 nm)/Pt(2 nm) layer stacks [Fig. 1(a)] on naturally oxidized Si substrates by means of magnetron sputtering at room temperature (base pressure 10^{-8} mbar; Ar is used as a sputter gas with a pressure of 10^{-3} mbar). To determine the micromagnetic parameters of the layer stack (Table I), we conduct an integral superconducting quantum interference device vibrating-sample magnetometry (SQUID VSM) and zero-offset anomalous Hall transport measurements [40]; see Fig. 1(b). The resulting out-of-plane (OOP) and in-plane (IP) hysteresis loops reveal the presence of a strong perpendicular magnetic anisotropy. Following the approach of Ref. [41], we estimate the exchange constant A based on the temperature dependence of the saturation

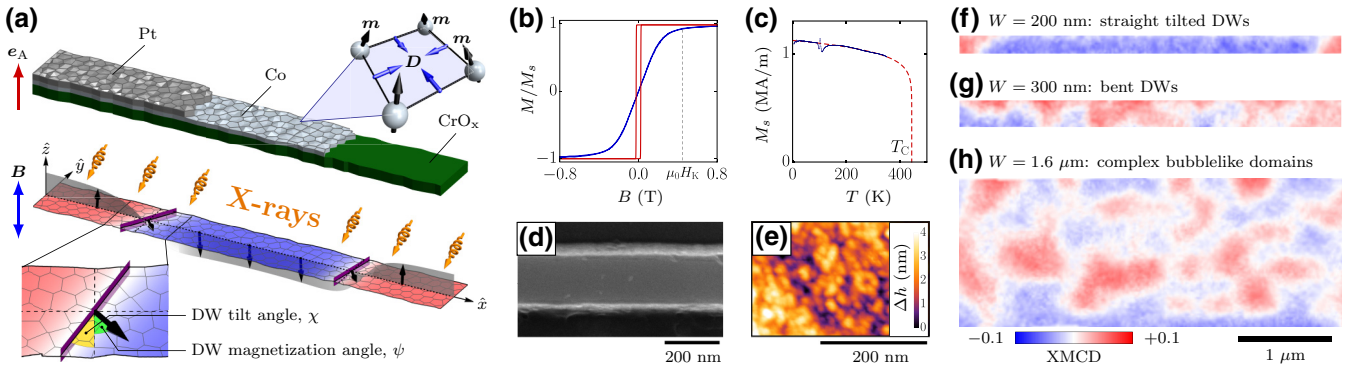

FIG. 1. Magnetic and structural investigations of nanostripes. (a) Schematic illustrations of a //CrO_x/Co/Pt asymmetric multilayer nanostripe after fabrication and the corresponding magnetic contrast with two tilted DWs. The angle between the DW plane and the $\hat{y}$ axis is the DW mechanical tilt angle χ, while the magnetization inside the DW is canted by the angle ψ with respect to the $\hat{y}$ axis. (b) The in-plane (blue) and out-of-plane (red) hysteresis loops of the magnetization normalized to the saturation magnetization M_s. (c) The temperature dependence of M_s obtained by means of SQUID VSM (blue). Red dashed line corresponds to the power law fitting: $M_s(T) = M_0\,(1 - T/T_C)^{\beta}$. (d) Scanning electron microscopy image of the patterned stripe with the width of 240 nm. (e) Atomic force microscopy image of the //CrO_x(5 nm)/Co(1.0 nm)/Pt(2 nm) stack. (f)–(h) Magnetic states imaged by XMCD PEEM for stripes of different widths W. Blue, white, and red contrasts correspond to magnetization vectors aligned along, perpendicular, and antiparallel to the x-ray beam, respectively.

TABLE I. Experimentally determined and estimated micromagnetic parameters of the sample.

Quantity	Value
Coercive field	$B_s = 25 \pm 2$ mT
Anisotropy field	$B_K = 450 \pm 25$ mT
Saturation magnetization	$M_s = 1.00 \pm 0.06$ MA/m
Uniaxial OOP anisotropy	$K_0 = 0.85 \pm 0.10$ MJ/m^3
Curie temperature (estimated)	$T_C = 443$ K
Exchange constant	$A = 5.6 \pm 0.6$ pJ/m
DMI constant (transport)	$D_0 = 0.90 \pm 0.13$ mJ/m^2
DW damping (extracted)	$\alpha \geq 0.1$
DMI constant (extracted)	$D \geq 0.80$ mJ/m^2

magnetization M_s [Fig. 1(c)] in the frame of Bloch's $T^{3/2}$ law. The DMI constant D_0 is quantified from the spin-orbit torques obtained by means of harmonic analysis of the Hall signals at different fields [42,43]; see Appendix A for details.

Electron-beam lithography and ion-beam etching are used to fabricate narrow stripes with length $L = 100$ μm and various widths W from 0.2 to 2.1 μm; see Fig. 1(d). The resulting sample reveals the presence of a 3 nm line-edge roughness for narrow stripes. The morphological analysis is done by means of atomic force microscopy (AFM) and exhibited the island growing mechanism for the Co layer on the surface of CrO_x; see Fig. 1(e) and Appendix B for details. These islands have a lateral size of about 45 nm and introduce to the system a surface roughness of about 3 nm (root-mean-square deviation). These two sources of roughness result in a complex pinning landscape for DWs [41,44].

The static magnetization states are visualized by means of x-ray magnetic circular dichroism photoelectron emission microscopy (XMCD PEEM); see Figs. 1(f)–1(h) and Appendix C for details. The magnetic pattern depends on the stripe width: (i) in narrow stripes with widths up to 300 nm we observe straight DWs [see Fig. 1(f)]; (ii) stripes with widths of 300 nm reveal the presence of bent DWs [see Fig. 1(g)]; (iii) in the case of wide stripes, $W > 1$ μm, complex bubblelike domains are obtained [see Fig. 1(h)]. The presence of straight tilted DWs in equilibrium [24,39] and bubblelike domains [12] additionally confirms the presence of a pronounced surface-induced DMI in the //CrO_x/Co/Pt layer stack.

We perform a detailed analysis of the DW morphologies by repeatedly imaging magnetic states in 200 nm wide nanostripes after an ac demagnetization procedure; see Appendix C (Fig. 9). The maximum field is $B_1 = +25$ mT with a subsequent change to $B_2 = -21.5$ mT and a further sign-changing amplitude decrease of 14% at each step. The resulting DW count statistics as a function of DW tilt angles is summarized in Fig. 2 as a diagram of DW

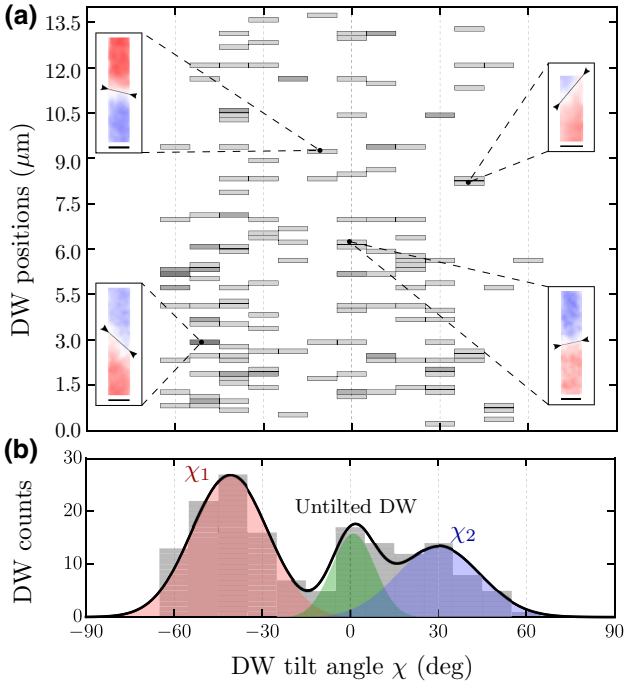

FIG. 2. Statistics of the experimentally obtained DW tilt angles. (a) Phase diagram of equilibrium DW morphologies for a ferromagnetic stripe with $W = 200$ nm extracted from the XMCD PEEM images after the ac demagnetization. Gray rectangles represent positions and corresponding tilts of DWs. (b) The corresponding distribution of DW counts versus the tilt angle χ.

positions with respect to the tilt angle χ. The vast majority of DW angles lie in the range $[-60°; +45°]$. In addition to the expected straight perpendicular to the $\hat{x}$-axis DW ($\chi = 0$), we observe two pronounced peaks at $\chi_1 = -34°$ ($\Delta\chi_1 = 10°$) and $\chi_2 = +22°$ ($\Delta\chi_2 = 10°$). We anticipate that the presence of these two characteristic tilt angles (χ_1 and χ_2) of opposite signs correlate with the two fields (B_1 and B_2) applied during the ac demagnetization procedure. This hints at the dynamic nature of the DW tilts upon their motion when exposed to the external magnetic field.

III. DISCUSSION

The appearance of tilted DWs in equilibrium could indicate the presence of a strong biaxial anisotropy in perpendicularly magnetized nanostripes [39]. In this case, the tilt of a DW plane appears due to the interplay between an additional in-plane easy-axis anisotropy and a surface-induced DMI. Using the formalism of Ref. [39], it can be shown that, for the material parameters summarized in Table I, the experimentally measured tilt angles cannot be obtained for any in-plane anisotropy satisfying the requirement that the sample has perpendicular magnetic anisotropy.

To understand the experimentally observed DW tilt in equilibrium, finite element micromagnetic simulations are performed for OOP magnetized stripes with a DMI of surface-induced type; see Appendix D for details. In numerical calculations, we examine not only homogeneous stripes with constant micromagnetic parameters (A, M_s, K_0, D, α), but also consider granular media. In the latter case, we assume that each grain has a different magnetic anisotropy that varies in the range $K_0 \pm \Delta K$, while the intergrain space has a constant value of anisotropy K_0. In the case of the homogeneous distribution of magnetic parameters in the medium or weak pinning ($\Delta K/K_0 \leq 10\%$), being exposed to an external OOP magnetic field, the DW starts moving and its plane acquires a tilt; see Fig. 3(a). The physical reason for this tilt is the interplay between the surface-induced DMI, which favors the Néel DW configuration, and the external magnetic field, which tends to rotate the magnetization away from the Néel configuration [24]. The subsequent relaxation of the tilted DW leads to the complete recovery of the equilibrium state with the DW plane being perpendicular to the $\hat{x}$ axis. For a moderately strong pinning ($10\% < \Delta K/K_0 < 20\%$), a moving DW remains straight and can be trapped in a tilted state after the external driving field B is switched off. This is due to pinning sites introduced by structural inhomogeneities, which create a complex energetic landscape for a DW. However, the discrete distribution of pinning sites leads to a distribution of the equilibrium tilting angles with a mean value given by the dynamic tilt. In the case of a strong pinning ($\Delta K/K_0 \geq 20\%$), the DW upon its motion acquires pronounced deformations in both dynamic and relaxed states. Direct comparison of the dynamics and statics of DWs for the two latter cases of pinning hints at the different physical natures of the pinning mechanism. The case of a moderately strong pinning ($10\% < \Delta K/K_0 < 20\%$) could be assigned to the line-edge roughness, as the DW plane remains straight without strong deformations, while the case in which $\Delta K/K_0 \geq 20\%$ corresponds to the strong influence of intergrain boundaries on the DW movement and relaxation.

A qualitative comparison of the experimentally obtained results with the micromagnetic simulations suggests that moderately strong pinning ($\Delta K/K_0 \approx 15\%$) is present in our samples as the DW plane remains straight. Quantitative statistical assessment of DW tilts from micromagnetic simulations is hardly possible as reasonable statistical analysis of a granular media requires a dramatic amount of time. Therefore, we base our further analysis on the collective coordinate approach [24,38], which describes the tilt of the DW upon its motion. By applying this model, which does not explicitly account for pinning of DWs, we rely on the fact that simulations reveal that the DW tilt angle upon its motion in the steady regime is similar to that in the relaxed state; see Fig. 3(a). The model is based on the assumptions that (i) pinning centers do not affect the DW dynamics; (ii) the DW plane remains rigid upon rotation [24,39], i.e.,

$$\cos\theta = -p\tanh\left[\frac{(x-q)\cos\chi + y\sin\chi}{\ell\Delta}\right],$$
$$\phi = \psi - 90^\circ, \tag{1}$$

where the polar θ and azimuthal ϕ angles are components of a spherical coordinate system introduced for the normalized magnetization vector $\mathbf{m} = \mathbf{M}/M_s = \{\sin\theta\cos\phi, \sin\theta\sin\phi, \cos\theta\}$, $\ell = \sqrt{A/K_3}$ is the magnetic length, $p = \pm 1$ is the DW polarity, χ is the tilt angle of the DW plane [see Fig. 1(a)], ψ is the DW magnetization angle in the DW with respect to the $\hat{y}$ axis, and Δ and q are the DW width and its center coordinate, respectively.

The total micromagnetic energy density $\mathcal{E} = \mathcal{E}_{\text{ex}} + \mathcal{E}_{\text{an}} + \mathcal{E}_{\text{DMI}} + \mathcal{E}_{\text{zeem}}$ includes the following four terms. (i) The exchange $\mathcal{E}_{\text{ex}} = A(\nabla m_i)(\nabla m_i)$ with $i = x, y, z$. (ii) Anisotropy $\mathcal{E}_{\text{an}} = -K_1 m_x^2 + K_3(1 - m_z^2)$ with $K_1 = 2\pi M_s^2 N_N$ and $K_3 = K_0 - 2\pi M_s^2(1 - 2N_N)$ being constants of the biaxial anisotropy that arise from the interplay between the uniaxial OOP anisotropy K_0 and shape-induced easy-axis anisotropy, which aligned along the $\hat{x}$ axis. The latter is defined by the demagnetization factor $N_N = H/(\pi W)\ln W/H + 3H/(2\pi W)$ for an infinitely long stripe with thickness H and width W [45,46]. (iii) The intrinsic DMI $\mathcal{E}_{\text{DMI}} = D[m_z(\nabla\cdot\mathbf{m}) - (\mathbf{m}\cdot\nabla m_z)]$. (iv) The Zeeman interaction $\mathcal{E}_{\text{zeem}} = -M_s B m_z$ with B being the intensity of the magnetic field.

In the case of the DW motion below the Walker limit, the set of equations for the collective coordinate model (1) could be derived from the Euler-Lagrange-Rayleigh equations (see Appendix E for details) and reads

$$\sin\chi = \frac{d\cos\psi}{2\sqrt{1 - k_1\sin^2\psi}}, \tag{2}$$

$$\Delta = \frac{1}{\sqrt{1 - k_1\sin^2\psi}}, \tag{3}$$

$$\dot{q} = \frac{2\omega_0 p\ell b}{\alpha\sqrt{4(1 - k_1\sin^2\psi) - d^2\cos^2\psi}}, \tag{4}$$

where $k_1 = K_1/K_3$ is the normalized in-plane anisotropy constant, $d = 2pD/D_c$ is the dimensionless parameter characterizing the DMI strength with $D_c = 4\sqrt{AK_3}/\pi$ being the value of the critical DMI [47], $b = BM_s/K_3$ is the normalized external magnetic field, and $\omega_0 = 2K_3\gamma/M_s$ is the characteristic frequency of the system with γ being the gyromagnetic ratio. The DW magnetization angle ψ can be determined by solving the algebraic equation

$$d\cos(\chi - \psi)\sqrt{1 - k_1\sin^2\psi} + k_1\sin(2\psi) + b/\alpha = 0, \tag{5}$$

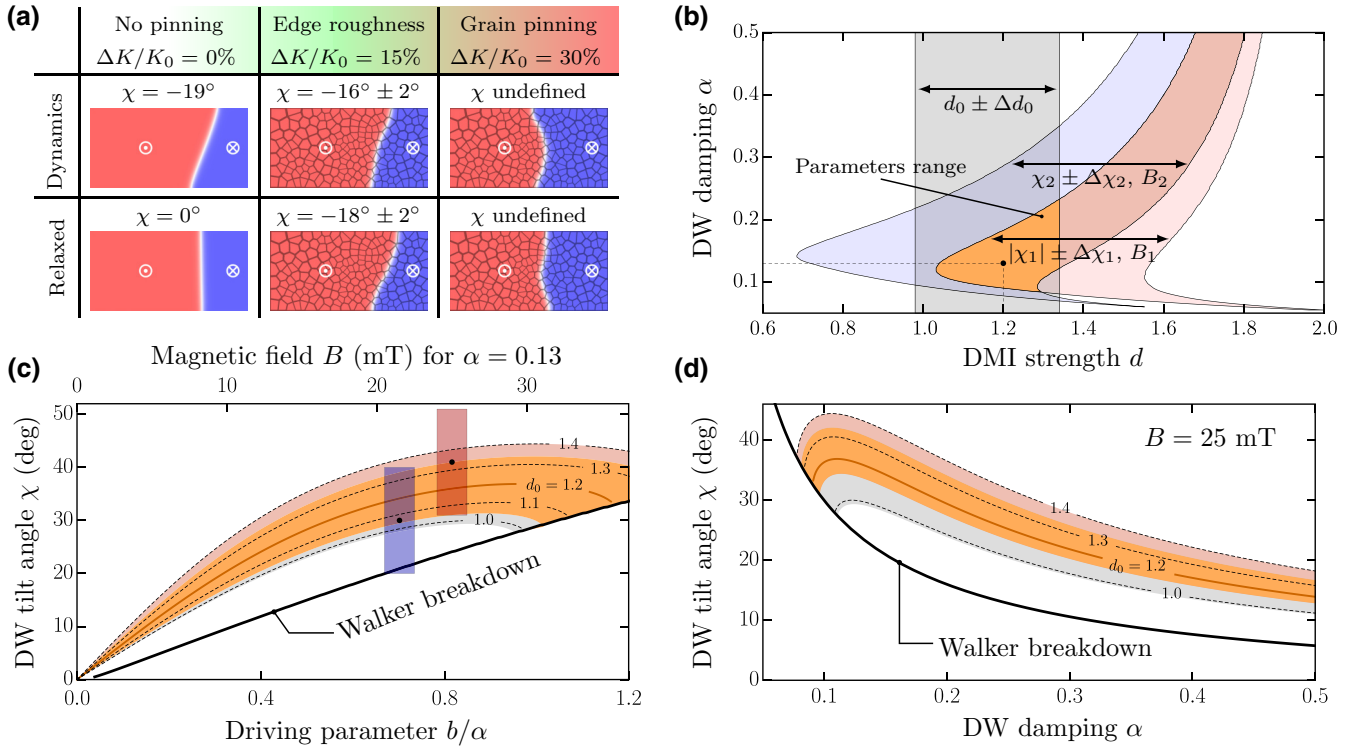

FIG. 3. Theoretical analysis of the DW tilt. (a) Micromagnetic simulation snapshots revealing the orientation of the DW in the homogeneous and granular media nanostripes being exposed to $B = 25$ mT. The upper row shows the dynamic state corresponding to the steady DW motion. The bottom row depicts the corresponding relaxed state. Stripe length $L = 200$ nm, width $W = 100$ nm, and thickness $H = 1$ nm. The DW tilt angle is defined from the linear interpolation of the isoline $m_z = 0$. (b) The parametric diagram of the DW tilts χ_1 and χ_2 in the space $\{d, \alpha\}$ for external fields B_1 and B_2. (c) The dependence of the DW tilt angle χ on the driving parameter b/α (bottom axis boundaries) and external magnetic field B for $\alpha = 0.13$ (top axis boundaries). Red and blue boxes represent the measured DW tilts $\chi_1 \pm \Delta\chi_1$ and $\chi_2 \pm \Delta\chi_2$ for external fields B_1 and B_2, respectively. (d) The tilt angle χ as a function of the damping parameter α at $B = 25$ mT.

which defines the crucial link between the DMI contribution and the driving parameter b/α. By solving Eq. (5) for the case of the experimentally applied magnetic fields $b_1 = B_1 M_s/K_3$ and $b_2 = B_2 M_s/K_3$, one could retrieve regions in the parameter space $\{d, \alpha\}$ that provide DW tilt angles from Eq. (2) in the experimentally determined range $|\chi_{1,2}| \pm |\Delta\chi_{1,2}|$; see Fig. 3(b). The overlapped region sets a boundary on the experimental parameters d and DW damping α that fulfil the DW tilts with the defined tilt angles for magnetic fields B_1 and B_2. The estimated DW damping parameter should be moderate, $\alpha \geq 0.1$, which is typical for asymmetric Co/Pt ultrathin sandwiches, where damping is dominated by the spin pumping mechanism [28,29]. Moreover, the estimated DMI constant should be rather strong, $d \geq 1.03$ ($D \geq 0.80$ mJ/m^2, being about half of the critical DMI value), to support the experimentally observed DW tilts. This estimation is in line with the DMI constant determined from the transport measurements (see Appendix A): $d_0 = 1.16 \pm 0.18$ ($D_0 = 0.90 \pm 0.13$ mJ/m^2). Using this DMI constant, it is also possible to refine the value for the DW damping from the experimentally determined parameter space: $\alpha = 0.13 \pm 0.02$.

In the spirit of Ref. [24], it is insightful to analyze the impact of the driving parameter b/α on the DW tilt for different strengths of the DMI; see Fig. 3(c). In line with previous investigations [24], higher critical velocities

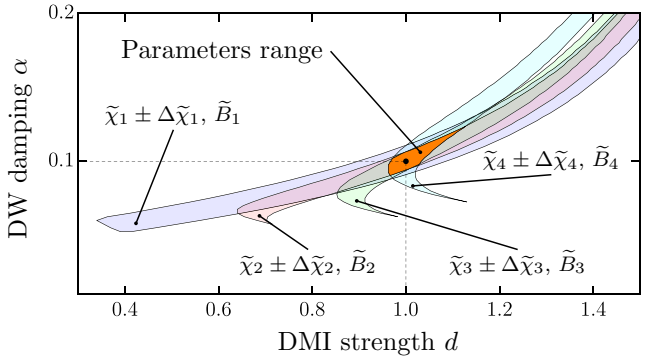

FIG. 4. Approach for the quantification of the DMI constant and the DW damping parameter. The range of the best fitting parameters α and d, which is defined as the overlapped region of determined ranges $|\widetilde{\chi}_i| \pm |\Delta\widetilde{\chi}_i|$ for the subsequent magnetic fields $\widetilde{B}_i$ with $i = \overline{1,4}$.

and larger DW tilt angles could be obtained for stronger DMIs. In the case when the external field is fixed and the damping parameter is known, these diagrams allow one to estimate the DMI constant, as was proposed in Ref. [24]. For instance, if we take DW damping $\alpha = 0.13$, the experimentally determined range of tilt angles give an estimate for $d \approx 1.1$ that corresponds to $D = 0.81$ mJ/m^2. In contrast, if d is known and the magnetic field is fixed, one could estimate the DW damping α based on the experimental measurements of the DW tilt angle; see Fig. 3(d).

It should be mentioned that the ranges of the DMI constant and DW damping parameter could be further restricted by additional sequences of measurement data: additional experimentally determined ranges of DW tilts $|\widetilde{\chi}_i| \pm |\Delta\widetilde{\chi}_i|$ with $i = \overline{1,4}$ for magnetic fields $\widetilde{B}_i$ lead to a significant shrinking of the overlapped region; see Fig. 4. This allows one to estimate experimentally undetermined parameters of the DMI strength d and DW damping α with higher accuracy.

IV. CONCLUSIONS

We present the experimental investigation of magnetic states in perpendicularly magnetized asymmetric //CrO_x/Co/Pt layer stacks with DMI. We show that the external magnetic field leads to the appearance of persistent tilted DWs that remain stable even when the field is switched off. We attribute the persistent tilt of the DWs to the pronounced pinning of DWs on structural inhomogeneities introduced by granular sample morphology. These defects are randomly distributed along the stripe and prevent the DW relaxation to the equilibrium state with the DW plane being perpendicular to the main stripe axis. Assuming magnetic anisotropy distribution between grains, we show that the line-edge roughness is the dominating source of pinning in the //CrO_x/Co/Pt system. The statistical analysis of the DW tilt angles after the specific field treatment can be self-consistently recalculated into the DW damping and DMI value by means of a theoretical formalism based on the collective coordinate approach. In our work, the utilization of two different magnetic fields allows us to determine the upper boundaries of DMI strengths $D \geq 0.80$ mJ/m^2 and DW damping parameters $\alpha \geq 0.1$. The combination of the proposed method with the standard magnetic metrological techniques allows us to refine the DMI constant $D = 0.93 \pm 0.03$ mJ/m^2 and the corresponding DW damping parameter $\alpha = 0.13 \pm 0.02$ for our system, which is in line with previous investigations of similar layer stacks [28,29]. The proposed approach could also be of advantage in studying asymmetric layer stacks without strong pinning. In this case, it will be necessary to perform dynamic microscopic investigations of the DW tilt at different fields or current densities.

Our work provides a simple yet robust approach for determining the DW damping and DMI constant, which are crucial not only for the application-oriented community, but also for the community working on the theory and micromagnetism. Namely, both these quantities enter as key parameters in all micromagnetic properties, including DW velocity and period of the Dzyaloshinskii spiral. Therefore, the possibility to assess these parameters simultaneously relying on conventional static experiments is invaluable for the community working on the theory and micromagnetism of chiral magnetic textures in ultrathin asymmetrically sandwiched ferromagnetic films.

ACKNOWLEDGMENTS

The authors thank Claudia Neisser and Diana Isabel Sandoval Bojorquez (HZDR) for the sample fabrication and Elfi Christalle (HZDR) for SEM measurements. The authors thank HZB for the allocation of synchrotron radiation beamtime. Support by the Ion Beam Center of HZDR is gratefully acknowledged. This work is financed in part via the German Research Foundation (DFG) under Grants No. MA5144/14-1, No. MA5144/22-1, No. MC9-22/1, and No. MA5144/24-1, and the Helmholtz Association of German Research Centres in the frame of the Helmholtz Innovation Lab "FlexiSens." This work is partially supported by Taras Shevchenko National University of Kyiv (Project No. 19BF052-01).

APPENDIX A: DMI CONSTANT QUANTIFICATION FROM TRANSPORT MEASUREMENTS

Spin-orbit torques (SOTs) can be used to control magnetization in asymmetric stacks of //CrO_x/Co/Pt [36,48–52]. The strength of the SOT can be assessed by measuring the effective magnetic field B_{SOT}, which introduces additional harmonic components to the measured Hall voltages [43]; see Figs. 5(a) and 5(b). To determine B_{SOT}, we prepare a lithographically patterned sample of an asymmetric //CrO_x(5 nm)/Co(1.0 nm)/Pt(2 nm) layer stack on a Si substrate with 300 nm oxide; see Fig. 5(a). The patterned Hall crosses of the sample have a width of 300 nm. The sample is driven at current densities up to $j = 2.3 \times 10^{11}$ A/m^2. To measure the effective field B_{SOT} of the antidamping SOT, the external magnetic field is applied in-plane (B_{IP}) perpendicular to the current flow direction. The measured Hall voltages and corresponding Hall resistances reveal the presence of the second harmonic signal; see Figs. 5(b) and 5(c). By sweeping the magnetic field, we retrieve the dependencies of the first and second harmonic signals of the Hall resistance, which allow us to quantitatively determine the strength of B_{SOT} from the relation [43]

$$B_{\mathrm{SOT}} = -2\frac{\partial R_H^{2\omega}/\partial B_{\mathrm{IP}}}{\partial^2 R_H^{\omega}/\partial B_{\mathrm{IP}}^2}, \tag{A1}$$

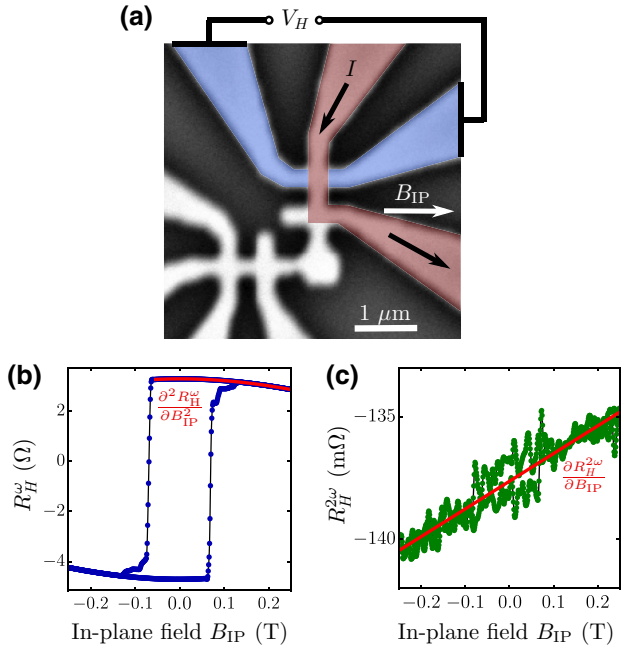

FIG. 5. Spin-orbit torque measurements. (a) Scanning electron microscopy image of the patterned Hall crosses. (b) The first and (c) second harmonic signals of the Hall resistance for the in-plane external magnetic field.

where R_H^ω and $R_H^{2\omega}$ are first and second harmonics of the Hall resistance. The resulting value of $B_{\mathrm{SOT}} = 1.67$ mT is used to estimate the DMI constant accordingly to the equation [42]

$$D_0 = \frac{2A\gamma}{v_s} B_{\mathrm{SOT}}, \tag{A2}$$

where $v_s = Pjg\mu_B/(2eM_s)$ is the spin velocity, with P being the spin polarization of the current, g being the Landé g factor, μ_B being the Bohr magneton, and e the electron charge.

The considered //CrO_x/Co/Pt system is complex due to its morphological structure and islands-growing mechanism of Co on the surface of CrO_x. This introduces an uncertainty about the degree of spin polarization in an electrical current, which is flowing along the Co/Pt interface. For instance, the spin polarization degree of Co is $P_{\mathrm{Co}} = 0.4$ [53], while the polarization of Pt in a Co/Pt system is $P_{\mathrm{Pt/Co}} = 0.2$, which is measured by means of spin polarized scanning tunneling microscopy [54]. The range of DMI constants, D_0, that corresponds to these spin polarizations is shown in Fig. 6. The actual value of the spin polarization has a quantitative impact on the DMI constant determined from the transport measurements, $D(P = 0.2) = 1.36$ mJ/m^2 and $D(P = 0.4) = 0.7$ mJ/m^2, due to the inverse dependence of the DMI constant D_0 on the spin polarization P. As the actual spin polarization in the //CrO_x/Co/Pt stack is loosely known, for our estimates,

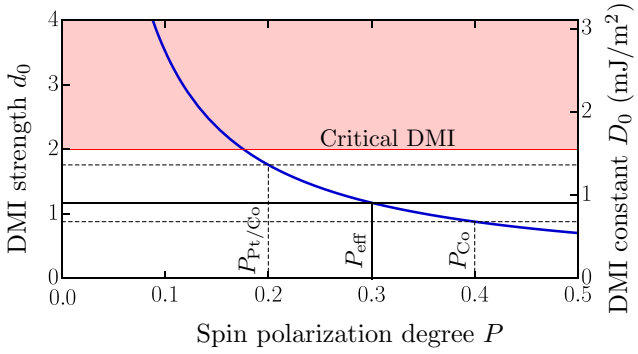

FIG. 6. Dependence of the DMI constant on the spin polarization degree. Blue line corresponds to Eq. (A2), which interconnects the DMI constant and spin polarization degree of the electrical current. Red region corresponds to the area above the critical DMI constant D_c where periodic spatially modulated magnetic states appear.

we assume that the electrical current acquires the effective spin polarization degree $P_{\mathrm{eff}} = 0.3$, which corresponds to the DMI constant $D_0^{\mathrm{eff}} = 0.9 \pm 0.13$ mJ/m^2 ($d_0^{\mathrm{eff}} = 1.16 \pm 0.18$). To generalize the consideration, we present here theoretical parametric diagrams of the DW tilts χ_1 and χ_2 in the space $\{d, \alpha\}$ and different ranges of d_0 quantified for $P_{\mathrm{Pt/Co}} = 0.2$ and $P_{\mathrm{Co}} = 0.4$; see Fig. 7.

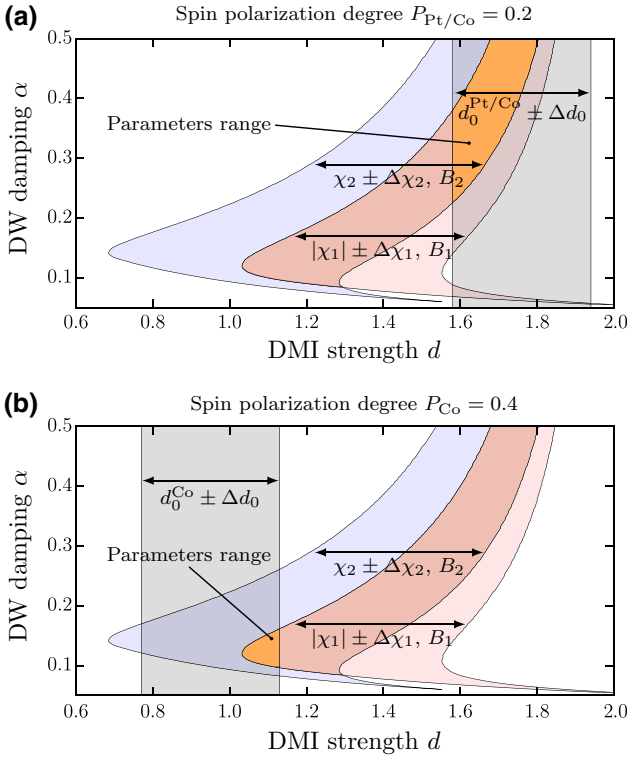

FIG. 7. (a),(b) Parametric diagrams in the space $\{d, \alpha\}$ for spin polarization degrees $P_{\mathrm{Pt/Co}} = 0.2$ and $P_{\mathrm{Co}} = 0.4$, respectively.

It should be noted that, for $P \geq 0.3$, we even have quantitative correspondence between the range of DMI constants quantified from our approach. For smaller values of the spin polarization, e.g., $P = 0.2$, the correspondence becomes only qualitative primarily due to the relatively large error bars on the determination of the DMI constant from transport measurements. Furthermore, we note that such small values of the spin polarization, e.g., $P < 0.2$, already bring the system to the critical DMI value ($D_c = 4\sqrt{A\,K_3}/\pi = 1.55$ mJ/m^2). For instance, the spin polarization degree $P_{\mathrm{Pt/Co}} = 0.1$ provides the strength of the DMI $D_0 = 2.7$ mJ/m^2, which is 74% higher than the critical DMI value. Such a strong DMI constant should cause the appearance of spatially periodic magnetic textures at remanence, which are not observed in our experiments. Thus, it provides us a hint that the spin polarization degree of the current in our system is at least not smaller than $P \sim 0.2$. In the case of $D_0 = 0.8$ mJ/m^2 and $P_{\mathrm{Pt}} = 0.1$, Eq. (A2) provides the value of the exchange constant $A = 1.64$ pJ/m, which is much smaller than that which we derive from the temperature dependence of the saturation magnetization [$A = 5.6 \pm 0.6$ pJ/m; see Fig. 1(c) and Table I].

APPENDIX B: MORPHOLOGICAL ANALYSIS OF THE CrO_x/Co/Pt FILM GROWTH

The magnetic properties of CrO_x/Co/Pt films are strongly dependent on the quality and thickness change of the Co layer. We therefore characterize the morphology of the films by means of AFM, which is carried out using a Bruker MultiMode8 instrument in tapping mode; see Fig. 8. To define the growth mechanism of Co on the surface of amorphous CrO_x, we additionally fabricate reference samples with //CrO_x(5 nm) and //CrO_x(5 nm)/Co(1.0 nm) layer stacks; see Fig. 8(a). The AFM image of the CrO_x layer grown at room temperature on naturally oxidized Si substrate reveals a flat surface with negligible topographical changes ($\Delta h^{\mathrm{rms}} = 0.37$ nm), which is important for the further growth of Co as the surface of CrO_x does not introduce any additional roughness to the stack. The AFM investigation of the Co layer on the surface of CrO_x detects the appearance of an island-like growing mode; see Fig. 8(b). The statistic distribution of grain counts versus their size reveals the presence of small (7.0 nm) and large (44.9 nm) grains with a maximum height of 4 nm; see Fig. 8(c).

APPENDIX C: XMCD PEEM MEASUREMENTS

The XMCD PEEM experiments are performed at the UE49PGMa beamline at the BESSY II synchrotron facility in Helmholtz-Zentrum Berlin [55] at the Co L_3 (777.2 eV) x-ray absorption edge, with the x-ray beam being incident at a grazing angle of 16°. The magnetic contrast is calculated through the intensities of photoemission electrons, I, that are emitted from the sample surface for left (I^-) and

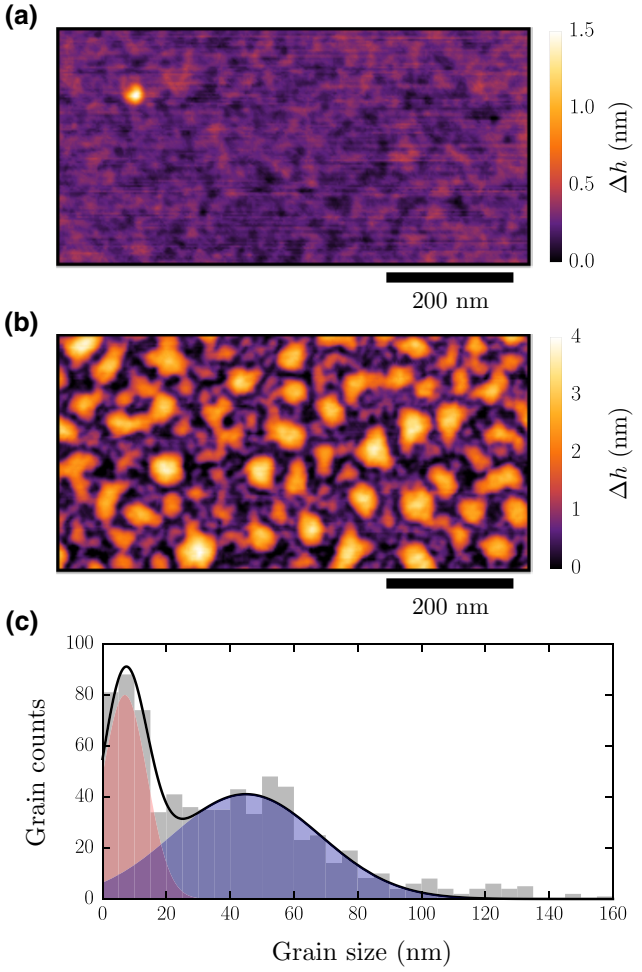

FIG. 8. AFM images and surface characterization. (a),(b) AFM micrographs of the reference samples //CrO_x(5 nm) and //CrO_x(5 nm)/Co(1.0 nm). (c) Co grain size distribution for the //CrO_x(5 nm)/Co(1.0 nm) multilayer system. The red and blue peaks correspond to the appearance of small and large grains with average dimensions 7.0 and 44.9 nm, respectively.

right (I^+) circular polarized x-rays:

$$\eta_{\mathrm{XMCD}} = \frac{I^+ - I^-}{I^+ + I^-}. \tag{C1}$$

The direction of the magnetic moment in the sample is depicted by blue, red, and white contrasts, which correspond to antiparallel, parallel, and perpendicular alignments of magnetic moments with respect to the incident x-ray beam.

The magnetic state of the sample structures is controlled through the out-of-plane magnetic field in the range [−25; +25] mT, which is generated by means of a solenoid electromagnet integrated in the sample holder. To investigate the magnetization change in nanostripes, an external magnetic field with a specific demagnetization sequence is applied to the sample: the temporal field profile has a

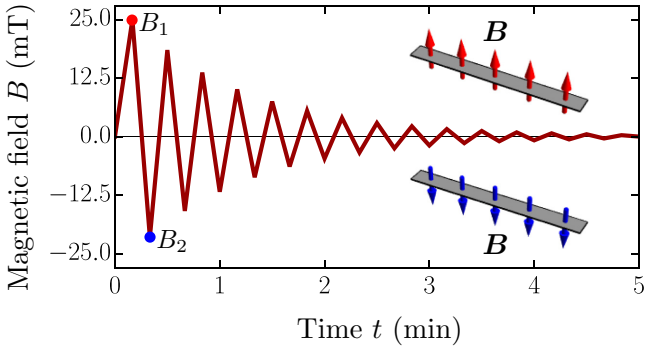

FIG. 9. Temporal profile of the external field. Dependence of the magnetic field applied to the sample on time. At each step the absolute field amplitude is reduced by 14%.

slowly alternating triangular waveform with a 14% reduction in the amplitude at each switching step; see Fig. 9. Namely, the maximum field is +25 mT (B_1 field), which is then followed by −21.5 mT (B_2 field), and so on. After applying this sequence, the magnetic state is visualized at remanence (static measurements) and compared with a previously observed one to detect the presence and morphology of tilted DWs in a stripe. The final distribution of the measured DW tilt angles and corresponding positions of DWs along the 200 nm wide stripe is presented in Fig. 2(a).

Since our experiments are performed in a static regime, we cannot comment on the direct correlation of the observed DW tilt angles with the applied external magnetic field. Still, in the case of a system with moderately strong pinning, only magnetic fields comparable with a coercive field B_s can alter the magnetic state of the stripe. Therefore, we believe that only B_1 and B_2 fields (strongest positive and strongest negative fields, respectively; see Fig. 9) result in the DW motion in the stripe.

APPENDIX D: DW MOTION AND RELAXATION IN GRANULAR MEDIA

The finite element micromagnetic simulations of the homogeneous and granular media are performed for the OOP magnetized nanostripes with 200 nm length, 100 nm width, and 1 nm thickness using the modified magnum.fe simulation package [56,57]. The granular media is introduced via a Voronoi mesh construction, where the averaged size of the grains is 20 nm with a 2 nm intercrystalline spacing. Simulations are performed for the material parameters close to the experiment (compare with Table I): exchange constant $A = 5.6$ pJ/m, saturation magnetization $M_s = 1.0$ MA/m, DMI constant $D = 0.5$ mJ/m^2, uniaxial OOP magnetic anisotropy $K_0 = 0.85$ MJ/m^2, and damping $\alpha = 0.2$. In the case of granular media, pinning centers are introduced to the magnetic system through the random variation of the magnetic anisotropy of the grains ($K_0 \pm \Delta K$), while in the internal spacing between grains the anisotropy is kept constant, K_0.

The micromagnetic simulations are done in the following way. (i) The initially relaxed DW starts moving along the stripe driven by the magnetic field $B_z = 25$ mT. (ii) Each micromagnetic snapshot from this motion is used as an initial state for the relaxation, thereby mimicking the relaxation process when the magnetic field is switched off. (iii) All dynamic and relaxed states of the DW are analyzed by means of linear interpolation of the $m_z = 0$ isoline. The resulting snapshots for the homogeneous and granular media are presented in Fig. 10. In the case of the homogeneous medium ($\Delta K/K_0 = 0\%$) and granular media with weak pinning ($\Delta K/K_0 = 0 \div 10\%$), the DW tilts only during its motion, while it relaxes to equilibrium with its plane being perpendicular to the stripe axis [24]. In the case of a moderately strong pinning ($\Delta K/K_0 = 15 \div 20\%$), the DW could be stabilized in a tilted state with the plane of the DW remaining straight. In the case of a strong pinning ($\Delta K/K_0 = 30\%$), the DW motion results in a strong deformation of the DW plane.

APPENDIX E: THEORETICAL MODEL

The normalized total energy for model (1) reads

$$\mathcal{E} = \frac{E}{E_0} = \frac{1}{\cos\chi}\left\{\frac{1}{\Delta} + \Delta\left[1 - k_1 \sin^2\psi\right] + d\sin(\chi - \psi) - bpq\cos\chi\right\}. \quad \text{(E1)}$$

The dynamics of the tilted DW follows the Euler-Lagrange-Rayleigh equations

$$\frac{\partial\mathcal{L}}{\partial\xi} - \frac{d}{dt}\frac{\partial\mathcal{L}}{\partial\dot{\xi}} = \frac{\partial\mathcal{F}}{\partial\dot{\xi}} \quad \text{(E2)}$$

with $\xi = q, \psi, \chi, \Delta$ and

$$\mathcal{L} = -\frac{M_s}{\gamma E_0} H \int dS\phi \sin\theta\dot{\theta} - E, \quad \text{(E3)}$$

$$\mathcal{F} = \frac{\alpha M_s}{2\gamma\omega_0 E_0} H \int dS\left[\dot{\theta}^2 + \sin^2\theta\dot{\psi}^2\right], \quad \text{(E4)}$$

where Eqs. (E3) and (E4) define the normalized Lagrangian and dissipative function of the system [58,59]. Here, α denotes the Gilbert damping of the magnetic system. The dot indicates the time derivative.

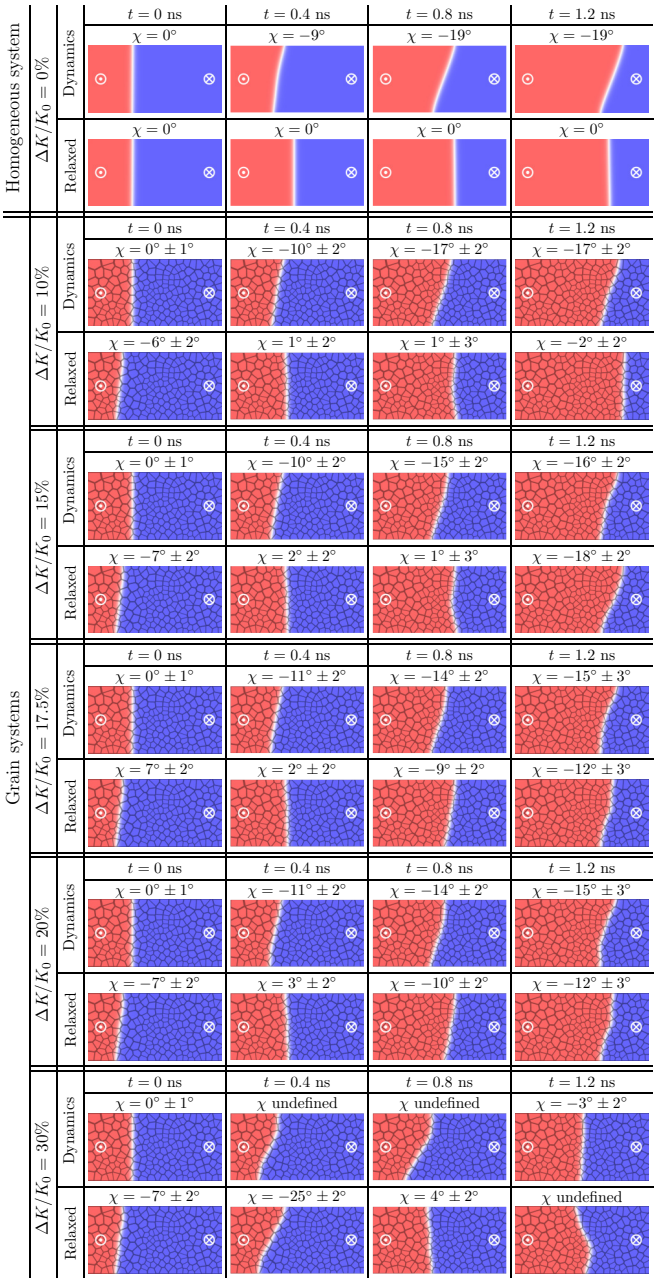

FIG. 10. Micromagnetic simulations of the homogeneous and granular media nanostripes. The upper row corresponds to the dynamic snapshot of the DW motion in the field $B = 25$ mT, while the bottom row depicts the corresponding relaxed state. Stripe length $L = 200$ nm, width $W = 100$ nm, and thickness $H = 1$ nm. The DW tilt angle is defined from the linear interpolation of the isoline $m_z = 0$.

Substituting Eqs. (E1), (E3), and (E4) into Eq. (E2) allows us to obtain the full set of equations for the collective variables:

$$-p\dot{q}\cos\chi + \alpha\Delta\dot{\psi} = k_1\Delta\sin(2\psi) + d\cos(\psi - \chi), \tag{E5}$$

$$p\dot{\psi} + \frac{\alpha}{\Delta}\dot{q}\cos\chi = pb, \tag{E6}$$

$$\frac{\alpha\pi^2}{12}\left[\frac{\dot{\Delta}}{\Delta} + \tan\chi\,\dot{\chi} + \frac{W^2}{\pi^2\ell^2\Delta^2}\frac{\dot{\chi}}{\sin(2\chi)}\right] = -\frac{d}{\Delta}\frac{\cos\psi}{\sin\chi} - \frac{1}{\Delta^2} - (1 - k_1\sin^2\psi), \tag{E7}$$

$$\frac{\alpha\pi^2}{12}\left[\frac{\dot{\Delta}}{\Delta} + \tan\chi\,\dot{\chi}\right] = -\frac{1}{\Delta^2} + (1 - k_1\sin^2\psi). \tag{E8}$$

Below the Walker limit, the equilibrium values of collective coordinates provide solutions (2)–(5) in the main text.

[1] A. Crépieux and C. Lacroix, Dzyaloshinsky–moriya interactions induced by symmetry breaking at a surface, J. Magn. Magn. Mater. **182**, 341 (1998).

[2] M. Bode, M. Heide, K. von Bergmann, P. Ferriani, S. Heinze, G. Bihlmayer, A. Kubetzka, O. Pietzsch, S. Blugel, and R. Wiesendanger, Chiral magnetic order at surfaces driven by inversion asymmetry, Nature **447**, 190 (2007).

[3] Hongxin Yang, André Thiaville, Stanislas Rohart, Albert Fert, and Mairbek Chshiev, Anatomy of Dzyaloshinskii-Moriya Interaction at Co/Pt Interfaces, Phys. Rev. Lett. **115**, 267210 (2015).

[4] Albert Fert, Nicolas Reyren, and Vincent Cros, Magnetic skyrmions: Advances in physics and potential applications, Nat. Rev. Mater. **2**, 17031 (2017).

[5] Roland Wiesendanger, Nanoscale magnetic skyrmions in metallic films and multilayers: A new twist for spintronics, Nat. Rev. Mater. **1**, 16044 (2016).

[6] I. Dzyaloshinsky, A thermodynamic theory of "weak" ferromagnetism of antiferromagnetics, J. Phys. Chem. Solids **4**, 241 (1958).

[7] Tôru Moriya, New Mechanism of Anisotropic Superexchange Interaction, Phys. Rev. Lett. **4**, 228 (1960).

[8] A. N. Bogdanov and D. A. Yablonskiĭ, Thermodynamically stable "vortices" in magnetically ordered crystals. The mixed state of magnets, Zh. Eksp. Teor. Fiz. **95**, 178 (1989).

[9] Naoto Nagaosa and Yoshinori Tokura, Topological properties and dynamics of magnetic skyrmions, Nat. Nanotechnol. **8**, 899 (2013).

[10] Seonghoon Woo, Kai Litzius, Benjamin Krüger, Mi-Young Im, Lucas Caretta, Kornel Richter, Maxwell Mann, Andrea Krone, Robert M. Reeve, Markus Weigand, Parnika Agrawal, Ivan Lemesh, Mohamad-Assaad Mawass, Peter Fischer, Mathias Kläui, and Geoffrey S. D. Beach, Observation of room-temperature magnetic skyrmions and their current-driven dynamics in ultrathin metallic ferromagnets, Nat. Mater. **15**, 501 (2016).

[11] William Legrand, Davide Maccariello, Nicolas Reyren, Karin Garcia, Christoforos Moutafis, Constance Moreau-Luchaire, Sophie Collin, Karim Bouzehouane, Vincent

Cros, and Albert Fert, Room-temperature current-induced generation and motion of sub-100 nm skyrmions, Nano Lett. **17**, 2703 (2017).

[12] W. Jiang, P. Upadhyaya, W. Zhang, G. Yu, M. B. Jungfleisch, F. Y. Fradin, J. E. Pearson, Y. Tserkovnyak, K. L. Wang, O. Heinonen, S. G. E. te Velthuis, and A. Hoffmann, Blowing magnetic skyrmion bubbles, Science **349**, 283 (2015).

[13] André Thiaville, Stanislas Rohart, Émilie Jué, Vincent Cros, and Albert Fert, Dynamics of dzyaloshinskii domain walls in ultrathin magnetic films, EPL (Europhysics Letters) **100**, 57002 (2012).

[14] Satoru Emori, Uwe Bauer, Sung-Min Ahn, Eduardo Martinez, and Geoffrey S. D. Beach, Current-driven dynamics of chiral ferromagnetic domain walls, Nat. Mater. **12**, 611 (2013).

[15] T. Schulz, R. Ritz, A. Bauer, M. Halder, M. Wagner, C. Franz, C. Pfleiderer, K. Everschor, M. Garst, and A. Rosch, Emergent electrodynamics of skyrmions in a chiral magnet, Nat. Phys. **8**, 301 (2012).

[16] Albert Fert, Vincent Cros, and Joao Sampaio, Skyrmions on the track, Nat. Nanotechnol. **8**, 152 (2013).

[17] Wanjun Jiang, Xichao Zhang, Guoqiang Yu, Wei Zhang, Xiao Wang, M. Benjamin Jungfleisch, John E. Pearson, Xuemei Cheng, Olle Heinonen, Kang L. Wang, Yan Zhou, Axel Hoffmann, and Suzanne G. E. te Velthuis, Direct observation of the skyrmion hall effect, Nat. Phys. **13**, 162 (2016).

[18] A. Neubauer, C. Pfleiderer, B. Binz, A. Rosch, R. Ritz, P. G. Niklowitz, and P. Böni, Topological Hall Effect in the a Phase of MnSi, Phys. Rev. Lett. **102**, 186602 (2009).

[19] Chirag Garg, See-Hun Yang, Timothy Phung, Aakash Pushp, and Stuart S. P. Parkin, Dramatic influence of curvature of nanowire on chiral domain wall velocity, Sci. Adv. **3**, e1602804 (2017).

[20] R. Tomasello, E. Martinez, R. Zivieri, L. Torres, M. Carpentieri, and G. Finocchio, A strategy for the design of skyrmion racetrack memories, Sci. Rep. **4**, 6784 (2014).

[21] Xichao Zhang, G. P. Zhao, Hans Fangohr, J. Ping Liu, W. X. Xia, J. Xia, and F. J. Morvan, Skyrmion-skyrmion and skyrmion-edge repulsions in skyrmion-based racetrack memory, Sci. Rep. **5**, 7643 (2015).

[22] Stefan Krause and Roland Wiesendanger, Spintronics: Skyrmionics gets hot, Nat. Mater. **15**, 493 (2016).

[23] Stuart Parkin and See-Hun Yang, Memory on the racetrack, Nat. Nanotechnol. **10**, 195 (2015).

[24] O. Boulle, S. Rohart, L. D. Buda-Prejbeanu, E. Jué, I. M. Miron, S. Pizzini, J. Vogel, G. Gaudin, and A. Thiaville, Domain Wall Tilting in the Presence of the Dzyaloshinskii-Moriya Interaction in Out-Of-Plane Magnetized Magnetic Nanotracks, Phys. Rev. Lett. **111**, 217203 (2013).

[25] Yaroslav Tserkovnyak, Arne Brataas, and Gerrit E. W. Bauer, Enhanced Gilbert Damping in Thin Ferromagnetic Films, Phys. Rev. Lett. **88**, 117601 (2002).

[26] Yaroslav Tserkovnyak, Arne Brataas, Gerrit E. W. Bauer, and Bertrand I. Halperin, Nonlocal magnetization dynamics in ferromagnetic heterostructures, Rev. Modern Phys. **77**, 1375 (2005).

[27] Arne Brataas, Yaroslav Tserkovnyak, and Gerrit E. W. Bauer, Scattering Theory of Gilbert Damping, Phys. Rev. Lett. **101**, 037207 (2008).

[28] J-M. L. Beaujour, J. H. Lee, A. D. Kent, K. Krycka, and C-C. Kao, Magnetization damping in ultrathin polycrystalline co films: Evidence for nonlocal effects, Phys. Rev. B **74**, 214405 (2006).

[29] A. J. Schellekens, L. Deen, D. Wang, J. T. Kohlhepp, H. J. M. Swagten, and B. Koopmans, Determining the gilbert damping in perpendicularly magnetized pt/co/AlOx films, Appl. Phys. Lett. **102**, 082405 (2013).

[30] F. Schreiber, J. Pflaum, Z. Frait, Th. Mühge, and J. Pelzl, Gilbert damping and *g*-factor in FexCo1-x alloy films, Solid State Commun. **93**, 965 (1995).

[31] J. A. Katine, F. J. Albert, R. A. Buhrman, E. B. Myers, and D. C. Ralph, Current-Driven Magnetization Reversal and Spin-Wave Excitations in co /cu /co Pillars, Phys. Rev. Lett. **84**, 3149 (2000).

[32] Ioan Mihai Miron, Thomas Moore, Helga Szambolics, Liliana Daniela Buda-Prejbeanu, Stéphane Auffret, Bernard Rodmacq, Stefania Pizzini, Jan Vogel, Marlio Bonfim, Alain Schuhl, and Gilles Gaudin, Fast current-induced domain-wall motion controlled by the rashba effect, Nat. Mater. **10**, 419 (2011).

[33] P. J. Metaxas, J. P. Jamet, A. Mougin, M. Cormier, J. Ferré, V. Baltz, B. Rodmacq, B. Dieny, and R. L. Stamps, Creep and Flow Regimes of Magnetic Domain-Wall Motion in Ultrathin Pt/Co/Pt Films with Perpendicular Anisotropy, Phys. Rev. Lett. **99**, 217208 (2007).

[34] J. Gorchon, S. Bustingorry, J. Ferré, V. Jeudy, A. B. Kolton, and T. Giamarchi, Pinning-Dependent Field-Driven Domain Wall Dynamics and Thermal Scaling in an UltrathinPt/co/PtMagnetic Film, Phys. Rev. Lett. **113**, 027205 (2014).

[35] Y. H. Choi, Y. Yoshimura, K-J Kim, K. Lee, T. W. Kim, T. Ono, C-Y. You, and M. H. Jung, Field-driven domain wall motion under a bias current in the creep and flow regimes in pt/[CoSiB/pt]n nanowires, Sci. Rep. **6**, 23933 (2016).

[36] Mohamed Belmeguenai, Jean-Paul Adam, Yves Roussigné, Sylvain Eimer, Thibaut Devolder, Joo-Von Kim, Salim Mourad Cherif, Andrey Stashkevich, and André Thiaville, Interfacial dzyaloshinskii-moriya interaction in perpendicularly magnetized pt/co/alo$_x$ ultrathin films measured by brillouin light spectroscopy, Phys. Rev. B **91**, 180405 (2015).

[37] M. Belmeguenai, M. S. Gabor, Y. Roussigné, A. Stashkevich, S. M. Chérif, F. Zighem, and C. Tiusan, Brillouin light scattering investigation of the thickness dependence of dzyaloshinskii-moriya interaction in $Co_{0.5}Fe_{0.5}$ ultrathin films, Phys. Rev. B **93**, 174407 (2016).

[38] A. P. Malozemoff and J. C. Slonzewski, *Magnetic Domain Walls in Bubble Materials* (Academic Press, New York, 1979).

[39] Oleksandr V. Pylypovskyi, Volodymyr P. Kravchuk, Oleksii Vokov, Juergen Fassbender, Denis Sheka, and Denys Makarov, Unidirectional tilt of domain walls in equilibrium in biaxial stripes with dzyaloshinskii-moriya interaction, J. Phys. D: Appl. Phys. **53**, 395003 (2020).

[40] Tobias Kosub, Martin Kopte, Florin Radu, Oliver G. Schmidt, and Denys Makarov, All-Electric Access to the Magnetic-Field-Invariant Magnetization of Antiferromagnets, Phys. Rev. Lett. **115**, 097201 (2015).

[41] Ivan A. Yastremsky, Oleksii M. Volkov, Martin Kopte, Tobias Kosub, Sven Stienen, Kilian Lenz, Jürgen Lindner, Jürgen Fassbender, Boris A. Ivanov, and Denys Makarov, Thermodynamics and Exchange Stiffness of Asymmetrically Sandwiched Ultrathin Ferromagnetic Films with Perpendicular Anisotropy, Phys. Rev. Appl. **12**, 064038 (2019).

[42] Kyoung-Whan Kim, Hyun-Woo Lee, Kyung-Jin Lee, and M. D. Stiles, Chirality from Interfacial Spin-Orbit Coupling Effects in Magnetic Bilayers, Phys. Rev. Lett. **111**, 216601 (2013).

[43] K. K. Meng, J. Miao, X. G. Xu, Y. Wu, X. P. Zhao, J. H. Zhao, and Y. Jiang, Enhanced spin-orbit torques in MnAl/Ta films with improving chemical ordering, Appl. Phys. Lett. **110**, 142401 (2017).

[44] M. Kopte, U. K. Rößler, R. Schäfer, T. Kosub, A. Kákay, O. Volkov, H. Fuchs, E. Y. Vedmedenko, F. Radu, O. G. Schmidt, J. Lindner, J. Faßbender, and D. Makarov, The complete micromagnetic characterization of asymmetrically sandwiched ferromagnetic films, ArXiv e-prints (2017), 1706.09322.

[45] Valery Slastikov, Micromagnetism of thin shells, Math. Models Methods Appl. Sci. **15**, 1469 (2005).

[46] Yuri Gaididei, Arseni Goussev, Volodymyr P. Kravchuk, Oleksandr V. Pylypovskyi, J. M. Robbins, Denis Sheka, Valeriy Slastikov, and Sergiy Vasylkevych, Magnetization in narrow ribbons: Curvature effects, J. Phys. A: Math. Theor. **50**, 385401 (2017).

[47] S. Rohart and A. Thiaville, Skyrmion confinement in ultrathin film nanostructures in the presence of dzyaloshinskii-moriya interaction, Phys. Rev. B **88**, 184422 (2013).

[48] Ioan Mihai Miron, Gilles Gaudin, Stéphane Auffret, Bernard Rodmacq, Alain Schuhl, Stefania Pizzini, Jan Vogel, and Pietro Gambardella, Current-driven spin torque induced by the rashba effect in a ferromagnetic metal layer, Nat. Mater. **9**, 230 (2010).

[49] Ioan Mihai Miron, Kevin Garello, Gilles Gaudin, Pierre-Jean Zermatten, Marius V. Costache, Stéphane Auffret, Sébastien Bandiera, Bernard Rodmacq, Alain Schuhl, and Pietro Gambardella, Perpendicular switching of a single ferromagnetic layer induced by in-plane current injection, Nature **476**, 189 (2011).

[50] Kevin Garello, Ioan Mihai Miron, Can Onur Avci, Frank Freimuth, Yuriy Mokrousov, Stefan Blügel, Stéphane Auffret, Olivier Boulle, Gilles Gaudin, and Pietro Gambardella, Symmetry and magnitude of spin–orbit torques in ferromagnetic heterostructures, Nat. Nanotechnol. **8**, 587 (2013).

[51] Nam-Hui Kim, Dong-Soo Han, Jinyong Jung, Jaehun Cho, June-Seo Kim, Henk J. M. Swagten, and Chun-Yeol You, Improvement of the interfacial dzyaloshinskii-moriya interaction by introducing a Ta buffer layer, Appl. Phys. Lett. **107**, 142408 (2015).

[52] M. Vaňatka, J.-C. Rojas-Sánchez, J. Vogel, M. Bonfim, M. Belmeguenai, Y. Roussigné, A. Stashkevich, A. Thiaville, and S. Pizzini, Velocity asymmetry of dzyaloshinskii domain walls in the creep and flow regimes, J. Phys.: Condens. Matter **27**, 326002 (2015).

[53] R. J. Soulen Jr., J. M. Byers, M. S. Osofsky, B. Nadgorny, T. Ambrose, S. F. Cheng, P. R. Broussard, C. T. Tanaka, J. Nowak, J. S. Moodera, A. Barry, and J. M. D. Coey, Measuring the spin polarization of a metal with a superconducting point contact, Science **282**, 85 (1998).

[54] Focko Meier, Samir Lounis, Jens Wiebe, Lihui Zhou, Swantje Heers, Phivos Mavropoulos, Peter H. Dederichs, Stefan Blügel, and Roland Wiesendanger, Spin polarization of platinum (111) induced by the proximity to cobalt nanostripes, Phys. Rev. B **83**, 075407 (2011).

[55] Florian Kronast and Sergio Valencia Molina, SPEEM: The photoemission microscope at the dedicated microfocus PGM beamline UE49-PGMa at BESSY II, Journal of Large-Scale Research Facilities JLSRF **2**, 90 (2016).

[56] Magnum.fe simulation package.

[57] Claas Abert, Lukas Exl, Florian Bruckner, André Drews, and Dieter Suess, magnum.fe: A micromagnetic finite-element simulation code based on FEniCS, J. Magne. Magn. Mater. **345**, 29 (2013).

[58] W. Döring, Über die trägheit der wände zwischen weißschen bezirken, Zeitschrift für Naturforschung **3A**, 373 (1948).

[59] A. Thiaville, J. M. Garcia, and J. Miltat, Domain wall dynamics in nanowires, J. Magn. Magn. Mater. **242-245**, 1061 (2002).